International Journal of Fatigue 202 (2026) 109223

Contents lists available at ScienceDirect

International Journal of Fatigue

journal homepage: www.elsevier.com/locate/ijfatigue

Three-dimensional mapping of residual stresses and crack propagation in refill friction stir spot welded aluminium samples via synchrotron X-ray diffraction and X-ray micro-computed tomography

Matteo Bernardi [a,*], David Canelo-Yubero [b,*], Ting Chen [a], Uceu F.H. Suhuddin [a], Luciano Bergmann [a], Benjamin Klusemann [a,c]

[a] Helmholtz-Zentrum Hereon, Institute of Material and Process Design, Solid State Materials Processing, Max-Planck-Str. 1, Geesthacht 21502, Germany
[b] Helmholtz-Zentrum Hereon, Institute of Materials Physics, X-Ray Diffraction with Synchrotron Radiation, Max-Planck-Str. 1, Geesthacht 21502, Germany
[c] Leuphana University Lüneburg, Institute for Production Technology and Systems, Universitätsallee 1, Lüneburg 21335, Germany

ARTICLE INFO

Keywords:
Refill friction stir spot welding
Residual stress
Fatigue
Fatigue crack propagation
Synchrotron radiation

ABSTRACT

Refill Friction Stir Spot Welding (refill FSSW) shows strong potential to replace riveting in the aerospace industry. However, the complex deformation and thermal effects associated with this process lead to residual stresses that may influence the fatigue life of the joint. This study reveals for the first time the non-uniform residual stresses across the thickness of a refill FSSW aluminium joint using synchrotron X-ray radiation in combination with a conical slit cell. Clear differences can be observed in the stresses between the region subjected to plasticisation and that affected solely by heat input. A fatigue testing campaign on the aluminium joints demonstrated their high reproducibility and robustness. X-ray micro-computed tomography enabled the three-dimensional visualisation of fatigue crack nucleation and propagation morphology, the latter correlated with the tensile residual stresses in the weld area. The results can contribute to the development of more accurate fatigue life prediction models and improve the overall reliability of refill FSSW aluminium joints in engineering applications.

1. Introduction

The aerospace industry is increasingly prioritising the development of innovative joining technologies. This interest is driven by the necessity to replace traditional fastening methods with more cost-effective and lightweight alternatives, particularly in response to the growing demand for higher production rates and lower fuel consumption. To meet these demands, solid-state joining technologies, such as refill Friction Stir Spot Welding (refill FSSW), have emerged as promising alternatives for manufacturing large aeronautical structures, providing higher production efficiency without solidification defects common in fusion welding [1–3]. Developed and patented by Helmholtz-Zentrum Hereon [4], this process utilises a non-consumable tool with two rotating components, a probe and a shoulder, concentrically assembled with a stationary clamping ring. During the process, the stationary clamping ring holds the materials against the backing bar, while the rotating shoulder plunges into the sheets and the probe moves upwards, creating space for the plasticised material to fill. The process is then reversed and both probe and shoulder retract back to the surface of the material, forcing the material that was trapped in the cavity formed by the probe to refill the hole left by the shoulder. Fig. 1 provides a visual representation of the entire process scheme.

In order to successfully adopt this technology in the aerospace industry, a thorough understanding of the fatigue behaviour of refill FSSW joints is essential. However, the fatigue analysis of such joint presents specific challenges due to the complexity of the microstructure and the distribution of residual stresses in the weld zones [5]. In fact, residual stress is a key factor in determining the structural integrity and fatigue performance of materials; however, its internal nature makes an accurate measurement challenging. Traditional measurement techniques often struggle to fully capture the complexity of residual stresses, particularly in advanced joining processes where the microstructure is intricate [6]. Despite its growing application, the precise distribution of stresses within refill FSSW joints remains enigmatic. The intricate interplay of nonuniform plastic deformation, thermal gradients, heterogeneous material flow, and rapid microstructural changes

* Corresponding authors.
E-mail addresses: matteo.bernardi@hereon.de (M. Bernardi), david.canelo@hereon.de (D. Canelo-Yubero).

https://doi.org/10.1016/j.ijfatigue.2025.109223
Received 26 April 2025; Received in revised form 30 July 2025; Accepted 5 August 2025
Available online 6 August 2025

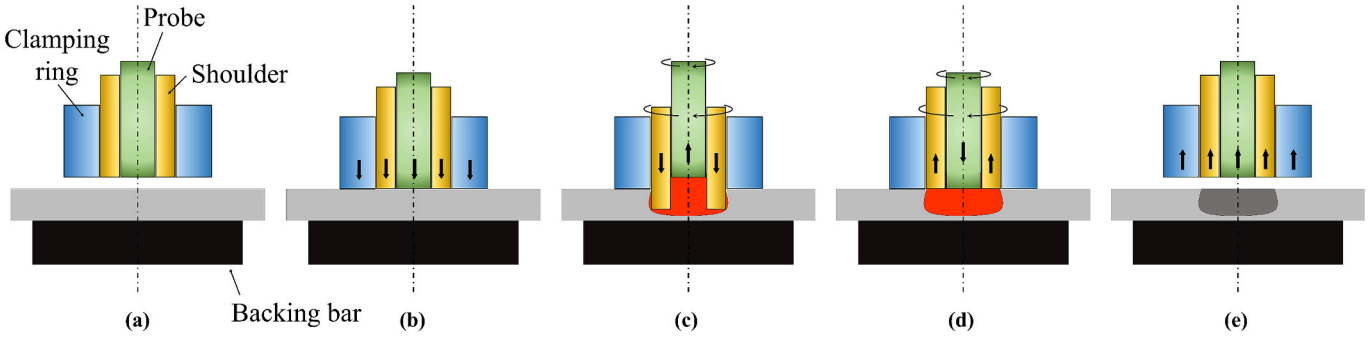

Fig. 1. Schematic illustration of refill FSSW process: (a) tool description, (b) clamping the material, (c) plunging the shoulder and retracting the probe, (d) returning the shoulder and probe to the material surface to refill the cavity, and (e) releasing the clamping force.

complicates the study of the stress field. However, this topic is of significant practical importance due to the impact of residual stresses on the overall mechanical performance of joints obtained by refill FSSW, as tensile stresses are known to adversely affect the fatigue behaviour [7–9] and stress corrosion cracking [10–12].

Synchrotron X-ray diffraction is a well-known technique for determining residual strains and stresses in engineering components [13–15]. Several studies have been conducted on refill FSSW to determine the residual stress field of the weld. However, simplifying assumptions, such as plane stress condition, were used, i.e. the presence of stresses in the direction of the specimen thickness was neglected [16–19].

The investigation of the influence of residual stresses on the fatigue behaviour of refill FSSW joints presents significant challenges, as the nucleation and propagation of fatigue cracks primarily occur within the material rather than on its external surfaces. This study employs X-ray micro-computed tomography (micro-CT) to provide a detailed analysis of the internal crack morphology. X-ray micro-CT is a 3D imaging technique that utilises X-rays to visualise the internal structure of materials. The X-ray micro-CT system records 2D X-ray images and reconstructs them into 2D cross-sectional slices, which are then processed to generate a complete 3D image. This process allows the acquisition of volumetric data that reveals changes in the internal microstructure and can be used to provide valuable insights into crack nucleation morphology, crack propagation paths and the effects of residual stresses on the fatigue life of the joint [20–22].

The present study focuses on a detailed experimental investigation of the fatigue behaviour of refill FSSW aluminium joints, specifically addressing the influence of different cyclic loading levels on crack growth and failure mechanisms. To address the limitations identified in previous investigations, a comprehensive three-dimensional (3D) analysis of the residual stress distribution in the aluminium joint was conducted, which, to the best of the authors' knowledge, represents the first of its kind. This stress analysis aims to demonstrate that the stresses present across the sample thickness are neither negligible nor uniform, as typically assumed. EBSD analysis was also used to correlate the material flow during the welding process with the resulting residual stress distribution.

2. Materials and methods

2.1. Material, welding conditions, and testing method

The RPS100 V32 welding machine by Harms & Wende GmbH was used for the welding procedure. The tool used was made of AISI M4 high-speed steel (ASTM A600) and comprised a clamping ring with a diameter of 17 mm, a shoulder with a diameter of 9 mm, and a probe with a diameter of 6 mm.

The material used for the joint is a 3 mm thick AA2219 T81 sheet; Table 1 summarises its chemical composition.

The weld was performed in a lap-joint configuration following ISO 14324:2003, using sheets measuring 185 × 60 × 3 mm with a 45 mm overlap. The welded sample was then cut to dimensions of 45 × 45 × 6 mm for residual stress analysis, with the weld positioned at the centre. The cutting was carried out using electrical discharge machining (EDM) to minimise mechanical and thermal influences on the residual stress state.

The welding parameters, summarised in Table 2, were optimised using a Design of Experiments (DoE) approach based on a Box–Behnken design, aiming to maximise the lap-shear strength of a single spot weld. The lap shear strength of the joint is 12 kN, obtained using a Zwick Z100 universal testing machine (Zwick-Roell, Germany) by testing three different samples at a speed of 1 mm/min.

The fatigue testing campaign was conducted using a Schenck servo-hydraulic testing machine (Schenck, Germany) equipped with a 10 kN load cell. To ensure repeatability, three samples were tested for 5 different load levels, expressed as a percentage of the lap-shear strength ($\%_{LSS}$). A stress ratio of 0.1 was applied in a sinusoidal waveform with a constant amplitude load at a frequency of 10 Hz. The two-parameter Weibull distribution was used to statistically analyse the fatigue test results, as it provides more conservative curves than other statistical distributions [23,24].

The Probability Density Function (PDF) is given by:

$$f(x) = \frac{\beta}{\alpha}\left[\frac{x}{\alpha}\right]^{\beta-1} e^{-\left[\frac{x}{\alpha}\right]^{\beta}} \quad (1)$$

where x represents the number of cycles to failure, α is the scale parameter and β the shape parameter, both strictly positive.

By integrating the PDF, the Cumulative Distribution Function (CDF) is derived as:

Table 2
Refill FSSW parameters.

Rotational speed (rpm)	Plunge depth (mm)	Plunge speed (mm/s)	Welding force (kN)
1500	3.4	0.8	15

Table 1
Chemical compositions of AA2219-T81 alloy (wt. %).

Si	Fe	Cu	Mn	Mg	Cr	Zn	Ti	Zr	V	Sn	Al
0.04	0.10	6.3	0.26	<0.01	<0.01	0.04	0.04	0.09	0.06	0.02	bal

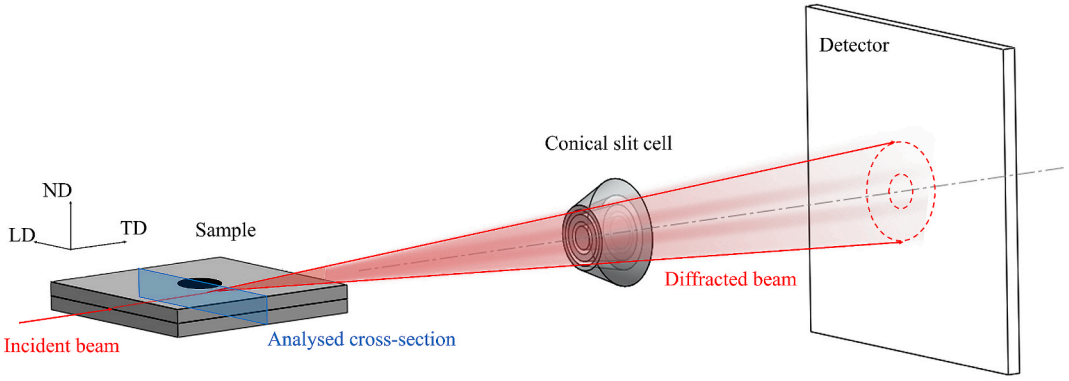

Fig. 2. Schematic drawing of the experimental setup used at the P07-HEMS beamline. The CSC allows a depth-resolved analysis within the sample.

$$F(x) = 1 - R(x) = 1 - e^{-\left[\frac{x}{\alpha}\right]^{\beta}} \quad (2)$$

R(x) is known as the reliability function, which corresponds to the survival probability of the specimens in fatigue testing.

Once the parameters α and β have been determined from the Weibull plot, the Mean Fatigue Life, also referred to as the Mean Time To Failure (MTTF), can be calculated. MTTF represents the expected number of cycles to failure under a specific stress level:

$$MTTF = \alpha\Gamma(1 + 1/\beta) \quad (3)$$

where $\Gamma(x) = (x-1)!$ is the gamma function.

The Coefficient of Variation (CV), which measures the relative variability of the dataset, is defined as the ratio of the Standard Deviation (SD) to the MTTF. These are calculated as:

$$SD = \alpha\sqrt{\Gamma(1 + 2/\beta) - [\Gamma(1 + 1/\beta)]^2} \quad (4)$$

$$CV = \frac{SD}{MTTF} = \sqrt{\frac{\Gamma(1 + 2/\beta)}{[\Gamma(1 + 1/\beta)]^2} - 1} \quad (5)$$

The fatigue life corresponding to different reliability values is calculated using:

$$N_{R_x} = \alpha[-\ln(R_x)]^{1/\beta} \quad (6)$$

where N_{R_x} represents the number of cycles to failure at a reliability level of R_x.

2.2. X-ray micro-CT and microscopy

Ex-situ X-ray micro-CT was used to examine the nucleation morphology and crack evolution during cyclic loading, providing a 3D visualisation of the crack shape. The scans were conducted using a Y. Cougar SMT micro-CT scanner (YXLON International GmbH, Germany), with a voltage of 70 kV and a current of 70 μA. The image reconstruction was performed with the myVGL software. After reconstruction, the images were analysed with Slicer software, and then SolidWorks was used to prepare the reconstruction of the volume-rendered image. One specimen of each failure mode was examined by stopping the fatigue test near failure.

For microstructural investigation, the specimen was mechanically polished and etched with Barker's etchant (1.8 % HBF_4 solution) and then examined by a LEICA DM-IRM optical microscope with polarised light to reveal the coloured grains. The fracture surface and macro/microstructure were examined using an FEI Quanta 650 field-emission scanning electron microscope (SEM), equipped with an EDAX electron backscattered diffraction (EBSD) detector. The EBSD data were obtained at 15 kV with a step size of 0.2 μm and examined using TSL OIM software. For EBSD analysis, the samples were polished using a Vibro-Met2 vibratory polisher (Buehler, Germany) with a 0.02 μm silica suspension.

2.3. Residual stress determination by high-energy X-ray diffraction

The residual stress field was determined using synchrotron X-ray radiation at the beamline P07-HEMS, operated by Helmholtz-Zentrum Hereon, at the synchrotron source PETRA III at Deutsches Elektronen-Synchrotron (DESY, Hamburg). The beam energy was set to 87.1 keV and a 2D (flat panel) Perkin-Elmer detector with an array of 2048 × 2048 pixels and a pixel size of 200 × 200 μm^2 was used to record the Debye-Scherrer rings. A conical slit cell (CSC) was used to provide a depth-resolved analysis within the bulk of the sample [14,25]. The CSC allows the definition of a gauge volume fixed in space. It consists of several concentric ring slits that, due to their conical shape, focus on a specific spot within the sample. The analysis of full diffraction rings enables the simultaneous determination of all strain components in the plane orthogonal to the beam. This setup allows the resolution to be customised depending on the beam energy and size. The Al-220 Bragg plane, weakly affected by intergranular strains [26], was analysed. This choice was imposed by the fixed energy of the single-bounce monochromator and the design of the CSC itself, which is designed to capture different Bragg planes of cubic lattices avoiding peak overlap while maintaining a focal distance of 100 mm. The incident beam cross-section was 0.3 × 0.3 mm^2 and the length of the gauge volume ~ 3 mm. Fig. 2 shows the schematic of the experimental setup. The sample-detector distance, determined with a LaB_6 calibration powder, was approximately 1.381 m. A comb sample, machined out across the weld with EDM, was used as a stress-free reference (also referred to as d_0 in the text), based on the assumption that the teeth of the comb do not retain macroscopic stresses [27]. The comb was measured fully in transmission geometry to increase the statistics in the relatively coarse base material. A suitable sanity check for the measured d_0 values is the cross-check between the comb and the application of theoretical boundary conditions, such as that the longitudinal components should be close to 0 MPa at the outer surfaces.

The 2D diffraction images were integrated in cakes of 20° (to provide high peak-to-background ratio) using the software Pydidas [28], a software developed at Helmholtz-Zentrum Hereon for X-ray diffraction data analysis. A Voigt function was used to fit the diffraction peaks. The $\sin^2\psi$ method was applied to increase the goodness of the calculations. The change in ψ is achieved without rotation of the sample through the use of the area detector (the angle ψ is defined between the scattering vector and the sample within the diffraction plane that is orthogonal to the incident beam). This methodology was applied to find the associate strain components in two orthogonal directions before the sample was rotated 90° so that the final strain components could be determined.

The volume average strain within a polycrystalline component is

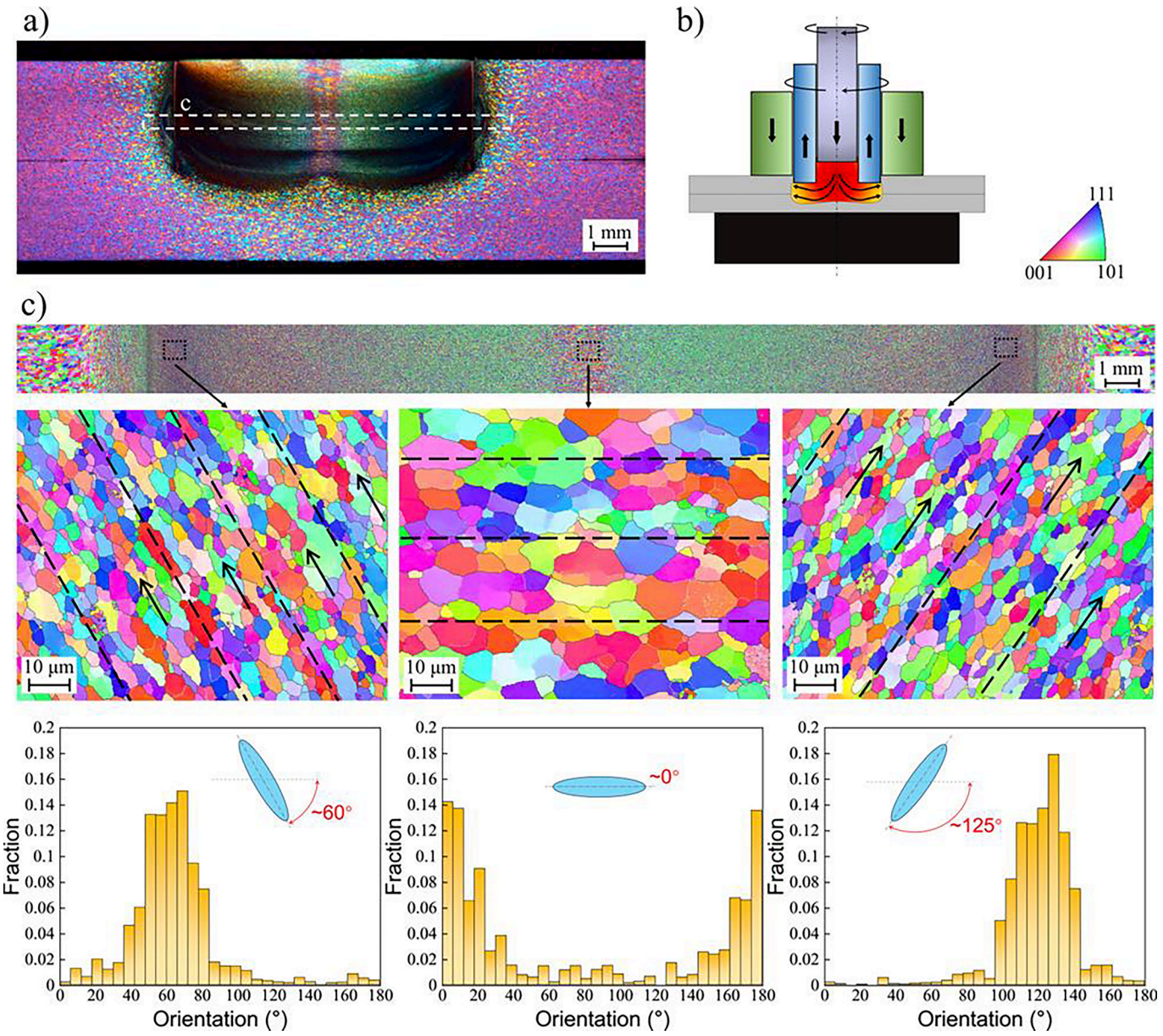

Fig. 3. (a) Optical image of the weld cross-section, (b) material flow scheme during the refill stage of the weld, and (c) EBSD maps and analysis of grain shape orientation at indicated locations in the weld.

determined, for the selected crystallographic plane as follows:

$$\varepsilon_i = \frac{(d_i - d_0)}{d_0} \tag{7}$$

where d_0 and d_i are the interplanar distances for the stress-free reference and the measured sample, respectively. The lower index *i* denotes the component parallel to the corresponding scattering vector. The *hkl* indexing is omitted for clarity of the expression. The triaxial stresses are computed using the generalised Hooke's law, where the stresses are calculated as follows:

$$\sigma_i = \frac{E}{1+\nu}\left[\varepsilon_i + \frac{\nu}{1-2\nu}(\varepsilon_{LD} + \varepsilon_{TD} + \varepsilon_{ND})\right] \tag{8}$$

where $E_{220} = 71.$GPa is the Young's modulus and $\nu_{220} = 0.347$ is the Poisson's ratio. ε_{xLD}, ε_{TD}, and ε_{ND} denote strains in longitudinal (LD), transverse (TD), and normal (ND) directions, respectively. This expression applies to the three orthogonal directions denoted with the lower index *i*. The elastic constants were calculated using the program by Wern et al. [29] based on the Kröner model [30]. The error bar reported for the stresses and presented in the results consists only of uncertainties propagated from the linear fit of the $\sin^2\psi$ method.

During the scanning, the sample was positioned with the axis of the weld perpendicular to the incident X-ray beam direction. The cross-section was scanned every 0.5 mm in both horizontal and vertical directions. The measurement was performed ensuring that the gauge volume remained completely inside the sample to avoid spurious strains.

3. Results and discussion

3.1. Three-dimensional residual stress determination and microstructure

Refill FSSW produces modifications in the microstructure of the material. Three different regions can be observed in the cross-section after the welding process, as shown in Fig. 3(a): Stir Zone (SZ), Thermo-Mechanical Affected-Zone (TMAZ), and Heat-Affected Zone (HAZ). The microstructure in the SZ is characterised by refined-

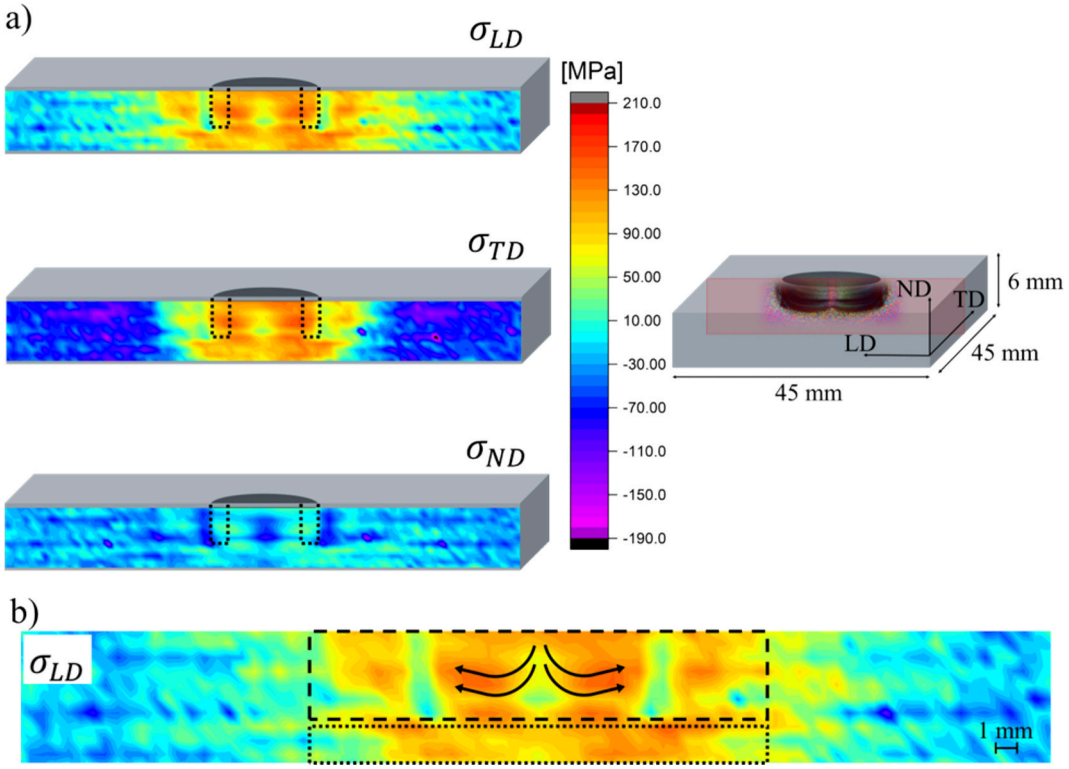

Fig. 4. (a) Residual stress determined along the cross-sections of the weld in the three orthogonal directions LD, TD, and ND; the dotted line represents the shoulder at the maximum plunge depth. (b) Enlarged view of the residual stress distribution in LD showing the material flow, the region affected by the shoulder plunge (dashed box), and the region only affected by the heat input (dotted box).

equiaxial grains, as a consequence of the dynamic recrystallisation due to the high temperatures reached and the considerable plastic deformation. The TMAZ is characterised by deformed and elongated grains, but dynamic recrystallisation is not observed due to the lower temperatures and the limited shear deformation. The HAZ is not affected by plastic deformation but the heat input during the process still affects the mechanical properties. Refill FSSW is unique among welding methods in its use of high force to refill material during the welding process, which leads to a complex material flow. During the refilling phase, the material flows from the inner part of the joint below the probe until it accumulates along the non-plasticised sides of the joint, as shown in Fig. 3(b). To validate this observation, an EBSD analysis of the joint cross-section was performed. Fig. 3(c) reveals that the grain shape orientation at the edges of the SZ is tilted by approximately 60°, while the grains in the central region of the joint exhibit no significant inclination. This analysis supports the hypothesis that, during the refilling phase, material flows into the zone vacated by the retracting shoulder, from the centre to the SZ edges. The same material flow behaviour was observed by Shen et al. [31]. Furthermore, the observed local texture could influence the residual stress determination, as it is well known that texture can affect the $\sin^2\psi$ method by causing oscillations in the diffraction data [32]. Nevertheless, the use of a crystallographic plane that is weakly affected by intergranular strains, combined with the presence of a moderate texture, resulted in linear $\sin^2\psi$ fits with no observable oscillations, indicating a negligible influence of texture on the stress determination.

Fusion welding processes generate residual stresses due to the constrained thermal expansion of the welded material by the adjacent and colder base material [33]. Although solid-state joining techniques avoid material melting, the heat generated during the process still introduces residual stresses in the material. For instance, in the case of friction stir welding (FSW), the peak value of these stresses is usually found between the HAZ and TMAZ [34]. The tool used in FSW typically consists of a shoulder and a conical probe, with minimal or no plunging variation during the welding process. However, in refill FSSW, the tool design is more intricate compared to conventional FSW, with two parts, the shoulder and the probe, that can move axially to refill the weld. Therefore, a plane stress assumption is not fully representative of the stress field since the plasticised region does not comprise the full thickness and a stress gradient is expected between the plasticised and non-plasticised region. Therefore, normal stresses have to be considered for a reliable stress determination. In Fig. 4(a), the determined stress field is shown in the three orthogonal directions: LD, TD, and ND. The average error bar is $\sim \pm 13$ MPa. In addition to the well-documented tensile stresses present in the welded area in both the LD and TD orientations, a notable stress component has been identified for the first time in ND. This stress component is compressive and surpasses 100 MPa in some regions. The maximum tensile stresses in the LD and TD align with the shoulder plunge location, while compressive stresses in ND exist on both the inner (probe region) and outer surfaces of the shoulder plunge area.

In Fig. 4(b), a detailed view of the stress distribution in LD is shown. It is interesting to note how the stress field differs between the region where the shoulder plunges (dashed box) and the area affected only by the heat input from the welding process (dotted box). A decrease in stresses is noticeable around the shoulder plunging location (indicated as a dashed line in Fig. 4(a)), attributed to the material flow occurring during the welding process. In this zone, plasticised material accumulates during the refilling stage, creating a compressive stress that counteracts the tensile stress caused by the heat during welding. This phenomenon is comparable to what occurs during rivet installation. It is well-documented in the literature that when a rivet is installed in a joint, it expands, generating compressive stress around the hole where it is applied [35,36]. In refill FSSW, a similar process occurs in a single operation. The plunging phase is analogous to the creation of a hole in a riveted joint, while the refilling phase is comparable to the rivet installation, which subsequently induces compressive stresses around

the hole. This hypothesis is supported by the material flow and the observation that the area not subjected to plasticisation by the welding tool does not exhibit this characteristic. Indeed, in this area, there is no variation in terms of stresses; only tensile stresses are present, which is similar to what is typically observed in fusion welding. This area is evident in the dotted box of Fig. 4(b) and the same phenomenon can also be observed in TD.

3.2. Fatigue behaviour

The fatigue life of the samples was assessed at five different maximum load levels, expressed as $\%_{LSS}$. Table 3 shows the fatigue test results. At the 10 $\%_{LSS}$, all three samples successfully reached 10 million cycles before the test was stopped and were therefore classified as run-outs. After testing, X-ray micro-CT indicated no observable crack nucleation in any of these samples. The fatigue curve is shown in Fig. 5 (a).

Table 3
Fatigue test results for a load ratio of 0.1. F_{max} is the maximum load, F_{min} is the minimum load, F_{mean} is the mean load and F_a is the load amplitude. N_f represents the number of fatigue cycles until failure of the samples. The tests were stopped at 10^7 cycles.

Load ($\%_{LSS}$)	F_{max} (kN)	F_{min} (kN)	F_{mean} (kN)	F_a (kN)	Cycles N_f
50 %	6.03	0.60	3.32	2.72	5,834
					8,279
					9,284
40 %	4.83	0.48	2.65	2.17	19,654
					22,045
					22,503
30 %	3.62	0.36	1.99	1.63	173,055
					192,739
					201,751
20 %	2.41	0.24	1.33	1.09	1,328,358
					1,382,983
					1,459,810
10 %	1.21	0.12	0.66	0.54	10,000,000
					10,000,000
					10,000,000

Table 4
Weibull parameters α and β, MTTF and CV for each load level.

Load ($\%_{LSS}$)	F_{max} (kN)	α	β	MTTF (cycles)	CV
50 %	6.03	8,608	3.910	7,792	0.29
40 %	4.83	22,147	12.651	21,264	0.10
30 %	3.62	195,997	12.130	187,896	0.10
20 %	2.41	1,421,718	20.116	1,384,247	0.06

Fig. 5(b) shows the CV versus the MTTF. The results demonstrate high reproducibility and robustness of the joints, with a CV below 30 % at the 50 $\%_{LSS}$ and around 10 % or less at the other loads. Particularly in the high-cycle fatigue region, which is critical for the fatigue design of an aeronautical component, the results are very consistent. These findings confirm the stability of the refill FSSW process, regardless of the material or the number of spots [37–39]. Table 4 summarises the Weibull parameters α and β, MTTF and CV used for the statistical analysis for each load level.

Fig. 5(c) presents the fatigue curves at two different reliability levels, 99 % and 50 %. As expected, the 99 % reliability level curve is similar to the 50 % reliability level curve, especially in the high-cycle fatigue region, due to the low coefficient of variation. The high reliability level results are essential for designers to estimate the fatigue life of a component.

3.3. Three-dimensional crack growth morphology and fracture surface analysis

The fatigue tests revealed two distinct failure modes depending on the level of applied load. Fig. 6 (a,b) shows the two different failure modes. At low loads (30 $\%_{LSS}$ and 20 $\%_{LSS}$), failure was observed in the bottom sheet. In contrast, at high loads (50 $\%_{LSS}$ and 40 $\%_{LSS}$),

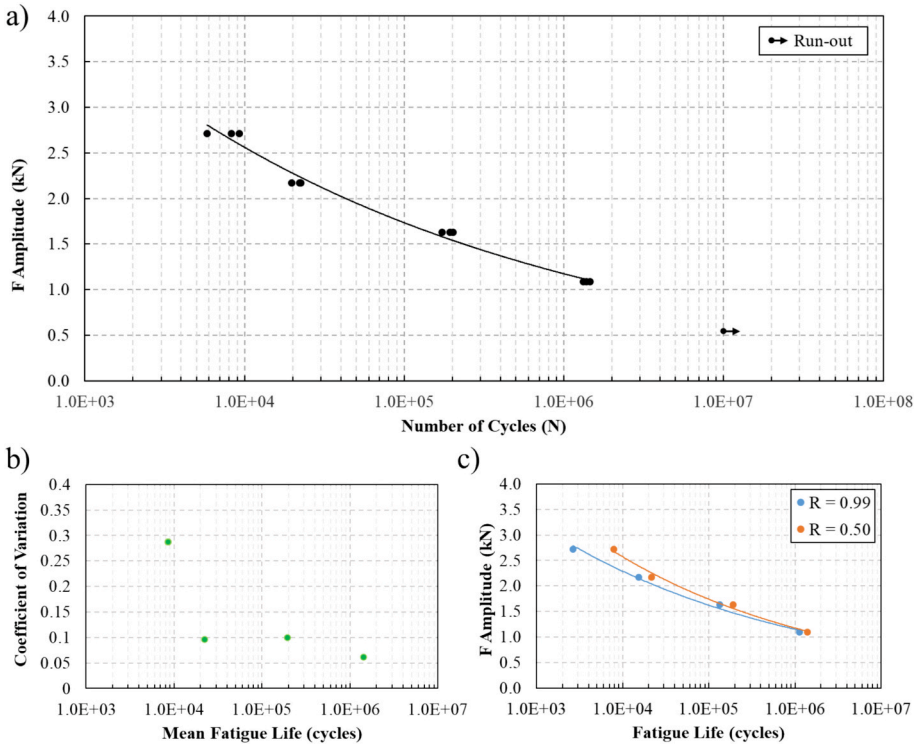

Fig. 5. (a) Fatigue curve with a run-out limit of 10 million cycles, (b) Coefficient of variation at different mean fatigue life, and (c) fatigue curves for reliability levels of 99% and 50%, showing high consistency of the results. The proximity between fatigue curves at different reliability levels in (c) reflects the low scatter in the fatigue data, particularly in the high-cycle fatigue regime.

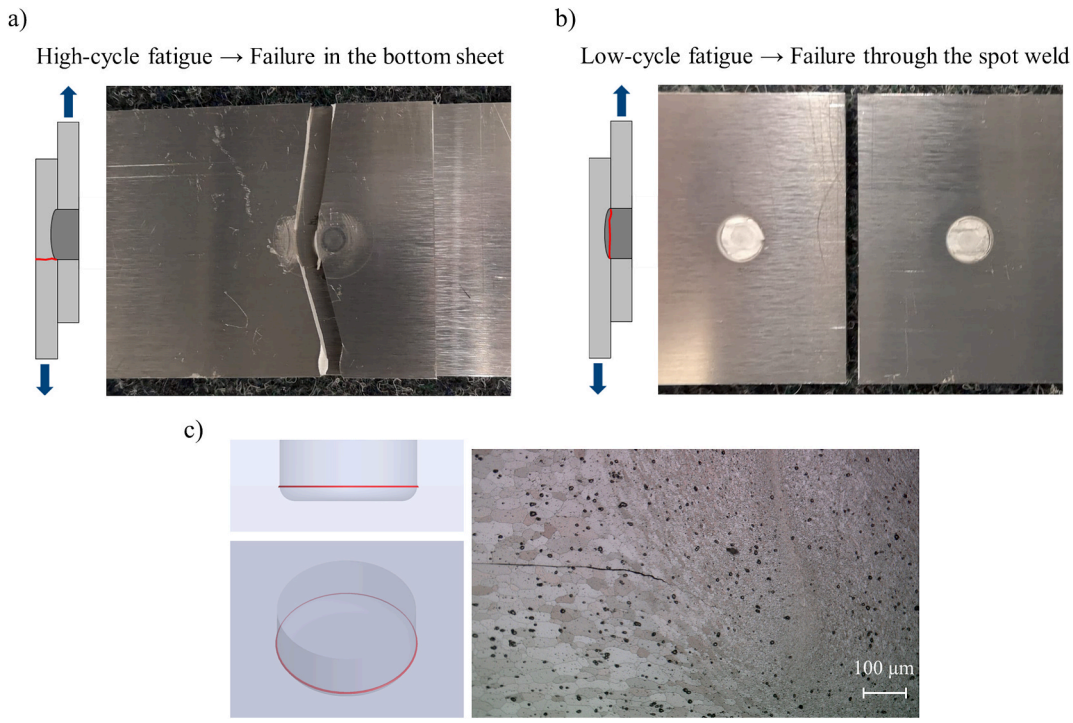

Fig. 6. (a) Failure in the bottom sheet under high-cycle fatigue (at 20%$_{LSS}$ and 30%$_{LSS}$). (b) Failure through the spot weld under low-cycle fatigue (at 40%$_{LSS}$ and 50%$_{LSS}$). (c) Isometric and lateral views of the "hook" location, and macrostructure of the spot weld showing the "hook".

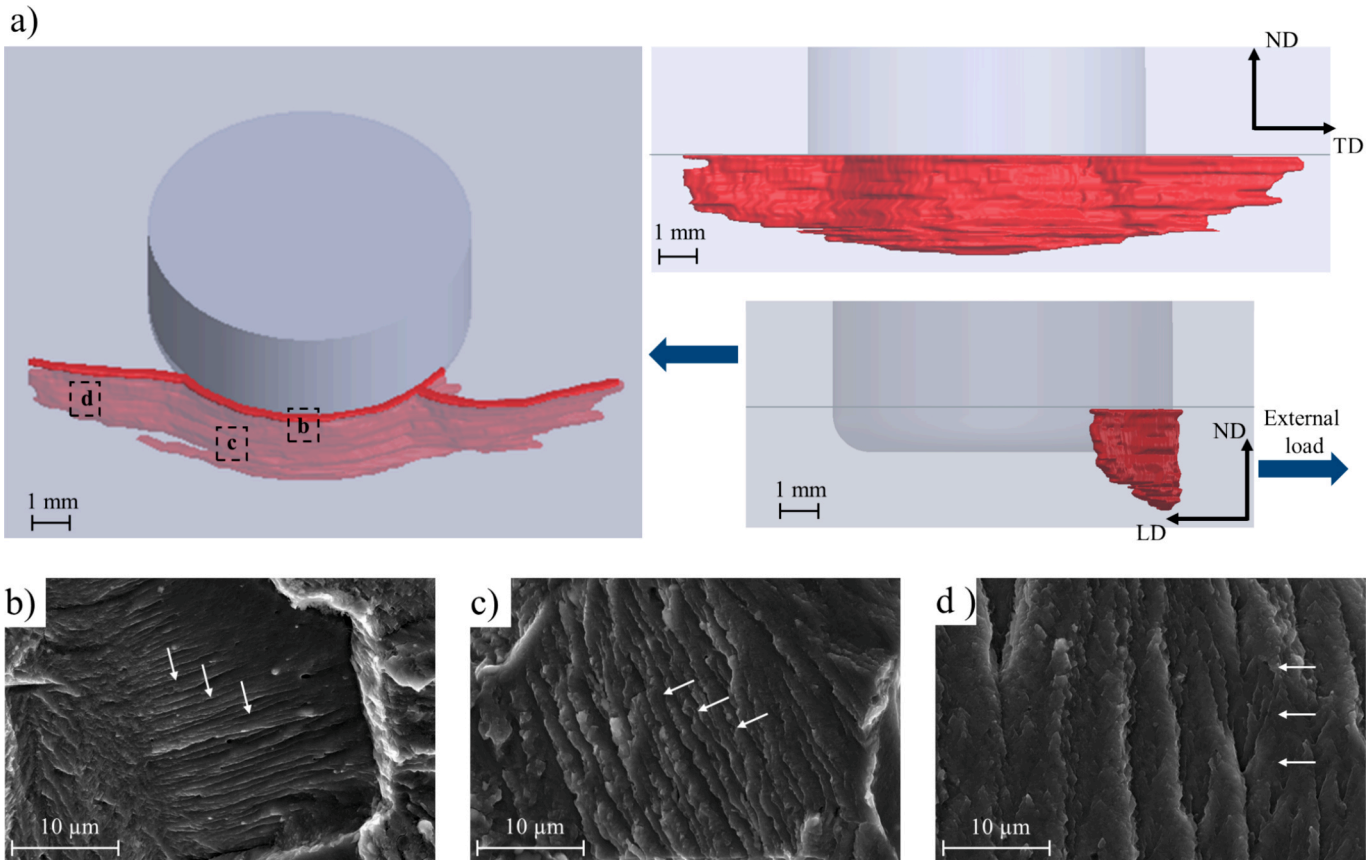

Fig. 7. (a) 3D X-ray micro-CT image showing the isometric, frontal, and lateral views of a fatigue crack in a sample tested at 20%$_{LSS}$ with 1,400,000 cycles. (b-d) SEM micrographs of the fracture surface; the white arrows indicate the crack propagation direction. The fatigue striations widen as the crack advances due to increasing stress from the reduced cross-section available to bear the external load.

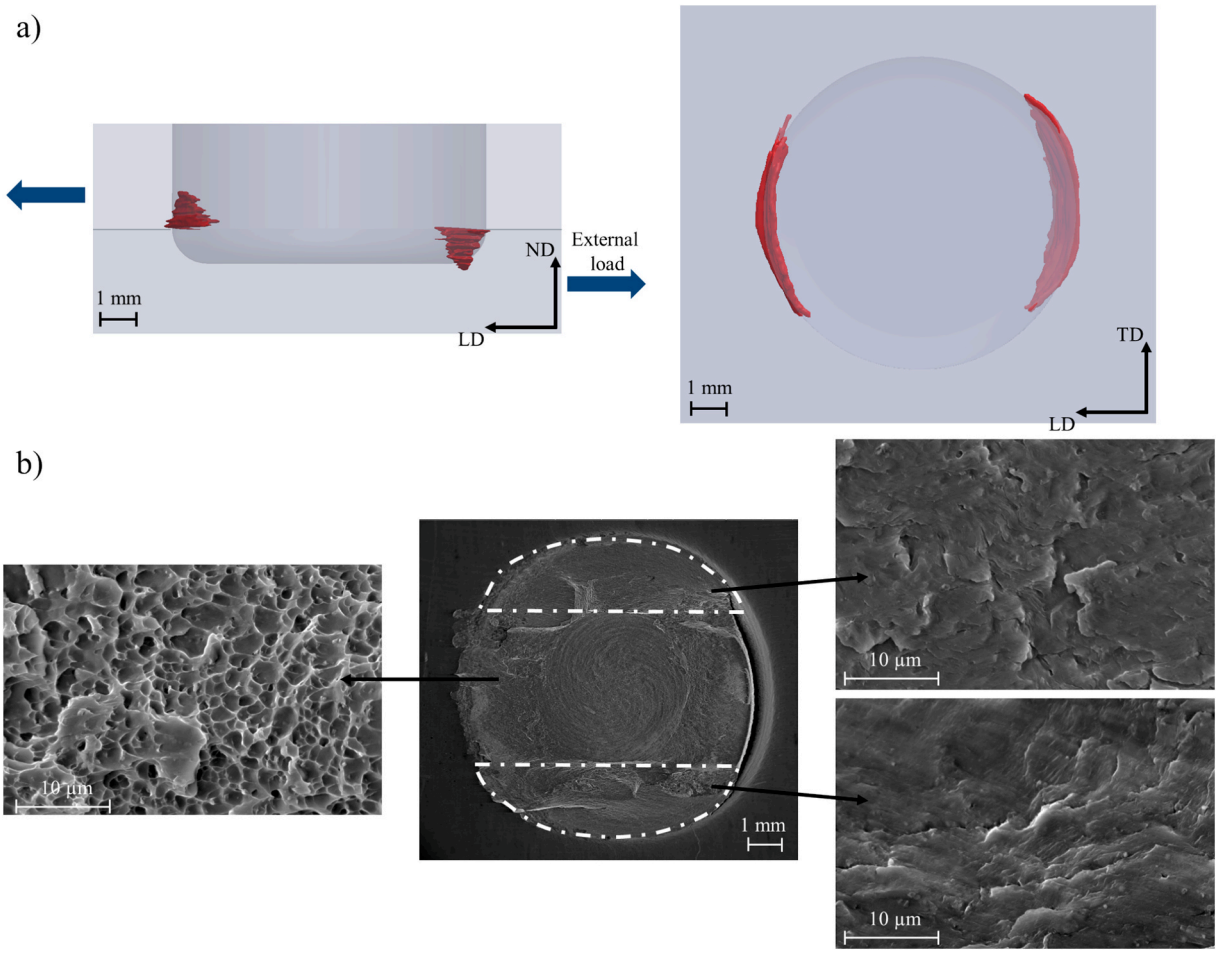

Fig. 8. (a) 3D X-ray micro-CT image of fatigue cracks in a sample tested at 40%$_{LSS}$ with 20,000 cycles. (b) SEM micrographs of the fracture surface. The white dashed line marks the fatigue crack propagation area. The dimples can be seen on the left.

corresponding to low-cycle fatigue, failure occurred through the spot weld.

The crack morphology for both failure modes was examined by stopping the fatigue test and using X-ray micro-CT. One sample at 40 %$_{LSS}$ with 20,000 cycles and another at 20 %$_{LSS}$ with 1.4 million cycles were investigated. After the X-ray micro-CT analysis, the samples were cut and prepared for EBSD, which confirmed the observations from X-ray micro-CT and provided further insights on the crack propagation in relation to the microstructure. Finally, SEM analysis of the fatigue fracture surfaces was conducted to better understand the failure mechanisms involved.

Unlike previous studies relying on 2D cross-sections or surface imaging [17], the use of X-ray micro-CT allowed the visualisation of complex, three-dimensional crack paths within the joint. This approach revealed multiple propagation directions and internal crack morphologies that would not have been detectable with traditional 2D techniques.

Fig. 7(a) illustrates the fatigue crack morphology of a sample tested at 20 %$_{LSS}$ after 1.4 million cycles. The actual 3D morphology of the fatigue crack growth was reconstructed, providing a more detailed understanding of its propagation behaviour. The crack nucleates from the so-called “hook”, a circumferential geometrical feature of refill FSSW that forms between the two sheets of the spot weld as a result of the tool plunging and retraction, as shown in Fig. 6(c). The crack propagates initially around the spot weld in ND and finally extends in the TD, see Fig. 7(a). The reconstructed crack shape aligns with the residual stress distribution, as the crack propagation is accelerated by the tensile stresses in the circumferential zone of the weld, confined by the lower tensile stresses outside the plunging area. The failure occurs in the bottom sheet, as shown in Fig. 6(a).

The SEM images of the fatigue striations reveal the progression of fatigue crack growth. In Fig. 7(b), during the initial stage, the crack propagates mainly towards the bottom sheet. In Fig. 7(c), it starts to spread around the spot weld and in Fig. 7(d), propagation becomes complete along the TD. The SEM micrographs also reveal that the fatigue striations are more closely spaced in the crack nucleation zone compared to the propagation zones. This is due to the constant test load combined with the decrease in cross-section as the crack advances, which causes an increase in stresses and thus wider fatigue striations.

The significance of the 3D crack morphology, as well as the knowledge of the 3D residual stress field, becomes even more evident when analysing crack propagation in a sample tested under low-cycle fatigue conditions. The X-ray micro-CT analysis of a sample tested at 40 %$_{LSS}$ with 20,000 cycles revealed two distinct cracks originating from the “hook”, one propagating towards the bottom sheet and the other extending towards the upper sheet, see Fig. 8(a). Although the presence of these two cracks may suggest the same failure mode as for high-cycle fatigue conditions, the actual failure of the sample occurred through the weld nugget. The presence of these two cracks, revealed by X-ray micro-CT, combined with the external load that induces significant secondary bending, resulted in additional crack nucleation at the edges of the weld nugget on the LD-TD plane, highlighted by the white dashed line in the SEM images of Fig. 8(b). These two fatigue cracks were not detected during X-ray micro-CT analysis, as they nucleate near the final failure of the specimen. In fact, once nucleated these cracks rapidly propagate within the SZ due to the high tensile residual stresses, reducing the area

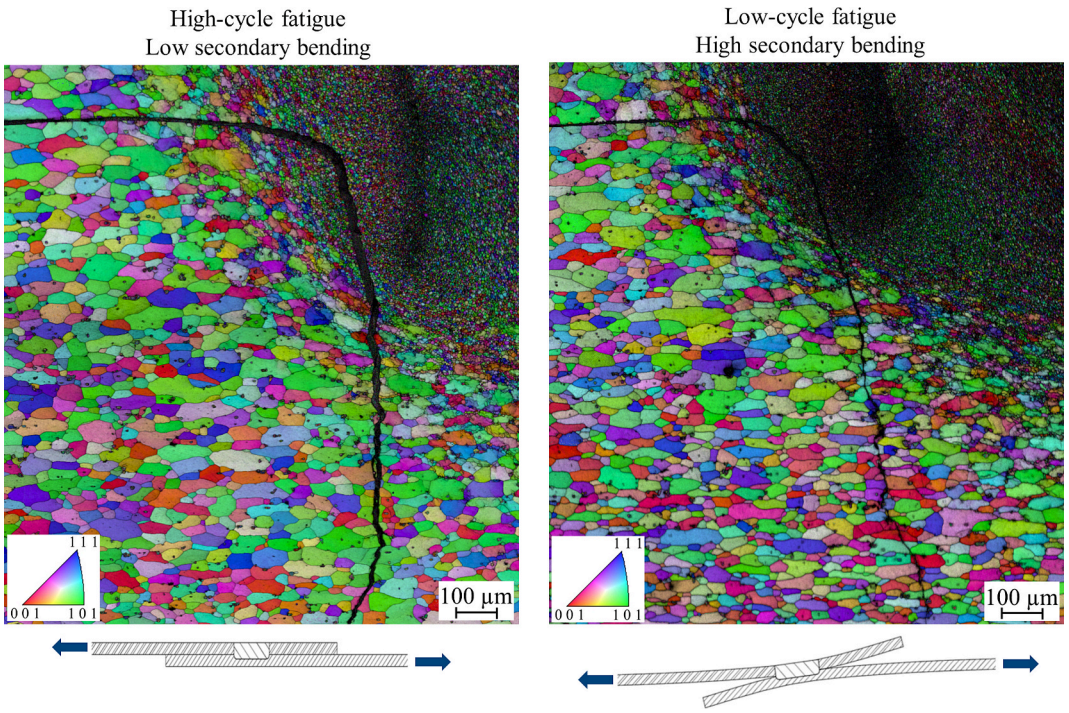

Fig. 9. EBSD map of the weld cross-section showing the crack propagation through the bottom sheet in case of low (left) and high (right) secondary bending. The schematic lab shear tests with secondary bending are simplified illustrations that clarify the concept for the reader.

available for load transfer until the weld fails at the centre of the spot, as indicated by the dimples in this region, see Fig. 8(b) on the left. Therefore, at high load levels, four fatigue cracks are observed: two along the ND direction, consistent with those seen under low load conditions, followed by two additional cracks that propagate in the TD–LD plane, ultimately leading to failure.

Another key observation is the influence of secondary bending on the crack propagation angle. The critical role of secondary bending in the fatigue performance of lap joints is well established in the literature [40,41]. In fact, Schijve et al. [42] demonstrated that, in lap joints, the secondary bending stress can exceed the stress induced by the external load, highlighting the crucial role of secondary bending in the fatigue behaviour of these joints. This phenomenon leads to different failure modes under varying load conditions, as previously discussed, and can also result in variations in the crack propagation path. Fig. 9 shows the crack propagation angles for both high-cycle and low-cycle fatigue samples. In the low-cycle fatigue sample, cracks exhibit a greater tendency to deviate towards the centre of the spot weld compared to those under lower fatigue loads. This deviation is a direct consequence of the sample deflection induced by secondary bending.

The insights gained from this study are highly relevant to engineering applications. X-ray micro-CT revealed that, under high-cycle fatigue conditions, cracks propagated primarily in the lower sheet, where the tensile residual stress was found to be higher than in the upper sheet around the weld. Although it is difficult to assess the exact influence of each parameter, the most plausible scenario would be that crack nucleation is mainly influenced by the “hook”, the crack propagation path depends more on the geometry, microstructure, and residual stresses of the joint, and the crack propagation rate is mainly affected by the residual stress field.

This highlights a potential risk in simplified engineering approaches that rely on residual stress measurements in transmission mode. Averaging through-thickness stress values can underestimate the actual residual stress in critical regions, potentially leading to non-conservative fatigue life predictions. This issue is particularly relevant for the aeronautical industry, where structures are designed using a damage-tolerant approach. In such safety–critical applications, underestimating crack growth due to inaccurate residual stress assumptions may compromise structural integrity and lead to catastrophic failure. The results presented in this study therefore provide essential input for improving the reliability of fatigue life predictions in refill FSSW joints, especially when considering their use as a potential alternative to conventional riveting.

4. Conclusions

This study provides a comprehensive analysis of the residual stress distribution and fatigue behaviour of refill FSSW aluminium samples. The findings demonstrate non-uniform residual stresses across the thickness of the welded sample, which have been largely neglected in previous studies that assumed plane stress conditions. The results show that the distribution of residual stresses in refill FSSW is more complex than previously observed, with notable compressive stresses in normal direction and clear differences between the regions affected by the shoulder plunge and those influenced only by heat input.

The fatigue life assessment demonstrated high reliability and consistency of refill FSSW aluminium joints, with a coefficient of variation below 30 % at high load levels and around 10 % or less at lower loads. Three-dimensional reconstruction of crack growth morphology provided new insights into distinct failure modes associated with different loading levels. At high loads (50 $\%_{LSS}$ and 40 $\%_{LSS}$), failure was observed through the weld nugget. However, this study revealed a much more complex failure behaviour, characterised by four distinct directions of fatigue crack propagation: two through the upper and bottom sheets, identified via X-ray micro-CT analysis, while the other two through the weld nugget, as confirmed by fracture surface analysis. The combination of reduced weld area and secondary bending eventually led to the failure of the weld nugget. At low loads (30 $\%_{LSS}$ and 20 $\%_{LSS}$), failure occurs in the bottom sheet, where the crack nucleates in a region with a high stress intensity factor, known as the “hook”, and propagates at an accelerated rate through the tensile residual stress zone surrounding the weld. Additionally, the effect of secondary bending on the angles of crack

propagation was observed. In low-cycle fatigue samples, cracks tend to deviate more towards the centre of the spot weld compared to those under lower fatigue loads.

CRediT authorship contribution statement

Matteo Bernardi: Writing – review & editing, Writing – original draft, Visualization, Validation, Methodology, Investigation, Formal analysis, Data curation, Conceptualization. **David Canelo-Yubero:** Writing – review & editing, Visualization, Validation, Methodology, Investigation, Formal analysis, Data curation, Conceptualization. **Ting Chen:** Writing – review & editing, Visualization, Validation, Formal analysis, Data curation. **Uceu F.H. Suhuddin:** Writing – review & editing, Validation, Supervision. **Luciano Bergmann:** Writing – review & editing, Supervision, Project administration. **Benjamin Klusemann:** Writing – review & editing, Supervision, Project administration, Funding acquisition.

Declaration of competing interest

The authors declare that they have no known competing financial interests or personal relationships that could have appeared to influence the work reported in this paper.

Acknowledgements

We would like to express our gratitude to the Deutsches Elektronen-Synchrotron DESY (Hamburg, Germany), which is a member of the Helmholtz Association HGF, for providing access to their experimental facilities. The work was carried out under grant number 20M2113H, which is funded by the German Federal Ministry of Economic Affairs and Climate Action (BMWK) under the LuFo VI-2 program. The authors would like to express their gratitude to Dr. Vasyl Haramus, from Helmholtz–Zentrum Hereon, for his assistance with the X-ray micro-CT equipment and the analysis of the results. Special thanks are also extended to Mr. Menno Peters, from Helmholtz–Zentrum Hereon, for his invaluable technical support throughout this work.

Originality Statement

I write on behalf of myself and all co-authors to confirm that the results presented in the manuscript are original and that neither the entire work nor any part of it has been previously published. The authors confirm that the article has not been peer-reviewed, nor has it been accepted for publication in another journal. The authors confirm that the research contained in the article is original and that all data provided are true and authentic. If necessary, the article may be revised and errors corrected.

Data availability

The data is available upon reasonable request from the corresponding author.

References

[1] Boldsaikhan E, Fukada S, Fujimoto M, Kamimuki K, Okada H. Refill friction stir spot welding of surface-treated aerospace aluminum alloys with faying-surface sealant. J Manuf Process 2019;42:113–20.
[2] Okada H, Kamimuki K, Fujimoto M. Assembly study of refill FSSW. SAE Int J Aerosp 2013;6:299.
[3] Su Y, Zhou M, Li W, Yang X, Shi Q, Xiong Y, et al. Microstructural evolution and mechanical behavior of TA5 titanium alloy joint in low-temperature friction stir welding with various cooling rates. Eng Fail Anal 2025;176:109667. https://doi.org/10.1016/j.engfailanal.2025.109667.
[4] Schilling C, dos Santos J. Method and device for joining at least two adjoining work pieces by friction welding. European Patent EP 1230062 B1 (WO 2001/036144); 1999.
[5] Xu Z, Li Z, Ji S, Zhang L. Refill friction stir spot welding of 5083-O aluminum alloy. J Mater Sci Technol 2018;34:878–85. https://doi.org/10.1016/j.jmst.2017.02.011.
[6] Mishra RS, Ma ZY. Friction stir welding and processing. Mater Sci Eng R Rep 2005;50:1–78. https://doi.org/10.1016/j.mser.2005.07.001.
[7] Fratini L, Pasta S, Reynolds AP. Fatigue crack growth in 2024-T351 friction stir welded joints: Longitudinal residual stress and microstructural effects. Int J Fatigue 2009;31:495–500. https://doi.org/10.1016/j.ijfatigue.2008.05.004.
[8] Hong S, Kim S, Lee CG, Kim S-J. Fatigue crack propagation behavior of friction stir welded Al–Mg–Si alloy. Scr Mater 2006;55:1007–10. https://doi.org/10.1016/j.scriptamat.2006.08.012.
[9] Pouget G, Reynolds AP. Residual stress and microstructure effects on fatigue crack growth in AA2050 friction stir welds. Int J Fatigue 2008;30:463–72. https://doi.org/10.1016/j.ijfatigue.2007.04.016.
[10] Van Boven G, Chen W, Rogge R. The role of residual stress in neutral pH stress corrosion cracking of pipeline steels. Part I: Pitting and cracking occurrence. Acta Mater 2007;55:29–42. https://doi.org/10.1016/j.actamat.2006.08.037.
[11] Zhang W, Fang K, Hu Y, Wang S, Wang X. Effect of machining-induced surface residual stress on initiation of stress corrosion cracking in 316 austenitic stainless steel. Corros Sci 2016;108:173–84. https://doi.org/10.1016/j.corsci.2016.03.008.
[12] Mochizuki M. Control of welding residual stress for ensuring integrity against fatigue and stress–corrosion cracking. Nucl Eng Des 2007;237:107–23. https://doi.org/10.1016/j.nucengdes.2006.05.006.
[13] Steuwer A, Peel MJ, Withers PJ. Dissimilar friction stir welds in AA5083–AA6082: the effect of process parameters on residual stress. Mater Sci Eng A 2006;441:187–96. https://doi.org/10.1016/j.msea.2006.08.012.
[14] Todt J, Keckes J, Winter G, Staron P, Hohenwarter A. Gradient residual strain and stress distributions in a high pressure torsion deformed iron disk revealed by high energy X-ray diffraction. Scr Mater 2018;146:178–81. https://doi.org/10.1016/j.scriptamat.2017.11.037.
[15] Malmelöv A, Hassila C-J, Fisk M, Wiklund U, Lundbäck A. Numerical modeling and synchrotron diffraction measurements of residual stresses in laser powder bed fusion manufactured alloy 625. Mater Des 2022;216:110548. https://doi.org/10.1016/j.matdes.2022.110548.
[16] Bernardi M, Suhuddin UFH, Fu B, Gerber JP, Bianchi M, Ostrovsky I, et al. Fatigue behaviour of multi-spot joints of 2024-T3 aluminium sheets obtained by refill Friction Stir Spot Welding with polysulfide sealant. Int J Fatigue 2023;172:107539. https://doi.org/10.1016/j.ijfatigue.2023.107539.
[17] Becker N, dos Santos JF, Klusemann B. Experimental investigation of crack propagation mechanism in refill friction stir spot joints of AA6082-T6. Eng Fract Mech 2024;300:109963. https://doi.org/10.1016/j.engfracmech.2024.109963.
[18] Yang X, Meng T, Su Y, Qi Z, Guo Z, Wu D, et al. Investigation on reducing residual stress and optimizing performance of 2219 aluminum alloy friction stir welded joint by cold spraying. J Manuf Process 2024;119:87–97. https://doi.org/10.1016/j.jmapro.2024.03.068.
[19] Becker N, Kuhn D, Piochowiak J, Klusemann B. Fatigue life enhancement via residual stress engineering due to local forming during refill friction stir spot welding. J Mater Res Technol 2025;36:2951–9. https://doi.org/10.1016/j.jmrt.2025.03.205.
[20] Han S, Yang N, Wang L, Abdel WM. Modelling of microscopic crack initiation behaviour of fretting fatigue based on X-ray micro-computed tomography scan. Int J Fatigue 2024;186:108374. https://doi.org/10.1016/j.ijfatigue.2024.108374.
[21] Han S, Dinh TD, De Baere I, Boone M, Josipovic I, Van Paepegem W. Study of the effect of defects on fatigue life prediction of additive manufactured Ti-6Al-4V by combined use of micro-computed tomography and fracture-mechanics-based simulation. Int J Fatigue 2024;180:108110. https://doi.org/10.1016/j.ijfatigue.2023.108110.
[22] Jiang L, Yang L, Yang B, Liao Z, Xiao S, Xiong H. Fatigue properties and damage evolution of CFRP/Al bolted joint under high load level using micro-CT technology. Int J Fatigue 2024;185:108360. https://doi.org/10.1016/j.ijfatigue.2024.108360.
[23] Khelif R, Chateauneuf A, Chaoui K. Statistical analysis of HDPE fatigue lifetime. Meccanica 2008;43:567–76.
[24] Zeng F, Yang Y, Qian G. Fatigue properties and S-N curve estimating of 316L stainless steel prepared by SLM. Int J Fatigue 2022;162:106946. https://doi.org/10.1016/j.ijfatigue.2022.106946.
[25] Staron P, Fischer T, Eims EH, Frömbgen S, Schell N, Daneshpour S, et al. Depth-Resolved Residual stress Analysis with Conical Slits for High-Energy X-Rays. Mater Sci Forum 2014;772:3–7. https://doi.org/10.4028/www.scientific.net/MSF.772.3.
[26] Hutchings MT, Withers PJ, Holden TM, Lorentzen T. Introduction to the Characterization of Residual stress by Neutron Diffraction. 1st ed. CRC Press; 2005.
[27] Taran YV, Balagurov AM, Schreiber J, Stuhr U. Residual stresses in a shape welded steel tube by neutron diffraction. J Phys Condens Matter 2008;20:104258. https://doi.org/10.1088/0953-8984/20/10/104258.
[28] Storm M, Lotze G. pydidas - Python Diffraction Data Analysis Suite 2025. Doi: 10.5281/zenodo.15038277.
[29] Wern H, Johannes R, Walz H. Dependence of the X-Ray Elastic Constants on the Diffraction Plane. Phys Status Solidi B 1998;206:545–57. https://doi.org/10.1002/(SICI)1521-3951(199804)206:2<545::AID-PSSB545>3.0.CO;2-J.
[30] Kröner E. Berechnung der elastischen Konstanten des Vielkristalls aus den Konstanten des Einkristalls. Z Für Phys 1958;151:504–18. https://doi.org/10.1007/BF01337948.
[31] Shen Z, Li WY, Ding Y, Hou W, Liu XC, Guo W, et al. Material flow during refill friction stir spot welded dissimilar Al alloys using a grooved tool. J Manuf Process 2020;49:260–70. https://doi.org/10.1016/j.jmapro.2019.11.029.

[32] Hauk V. Structural and Residual stress Analysis by Nondestructive Methods: Evaluation, Application, Assessment. Amsterdam, The Netherlands: Elsevier; 1997.
[33] Leggatt RH. Residual stresses in welded structures. Spec Issue Impact Second Residual Stress Struct Integr 2008;85:144–51. Doi: 10.1016/j.ijpvp.2007.10.004.
[34] Zapata J, Toro M, López D. Residual stresses in friction stir dissimilar welding of aluminum alloys. J Mater Process Technol 2016;229:121–7. https://doi.org/10.1016/j.jmatprotec.2015.08.026.
[35] Korbel A. Effect of aircraft rivet installation process and production variables on residual stress, clamping force and fatigue behaviour of thin sheet riveted lap joints. Thin-Walled Struct 2022;181:110041. https://doi.org/10.1016/j.tws.2022.110041.
[36] Zeng C, Xue JT, Liu XY, Tian W. Design variables influencing the fatigue of Al 2024-T3 in riveted aircraft lap joints: Squeeze force and initial fit tolerance. Int J Fatigue 2020;140:105751. https://doi.org/10.1016/j.ijfatigue.2020.105751.
[37] Effertz P, Infante V, Quintino L, Suhuddin U, Hanke S, Dos Santos J. Fatigue life assessment of friction spot welded 7050-T76 aluminium alloy using Weibull distribution. Int J Fatigue 2016;87:381–90.
[38] Homola P, Růžek R, McAndrew AR, De Backer J. Effect of primer and sealant in refill friction stir spot welded joints on strength and fatigue behaviour of aluminium alloys. Int J Fatigue 2023;168:107455. https://doi.org/10.1016/j.ijfatigue.2022.107455.
[39] Shen Z, Ding Y, Chen J, Gerlich AP. Comparison of fatigue behavior in Mg/Mg similar and Mg/steel dissimilar refill friction stir spot welds. Int J Fatigue 2016;92:78–86. https://doi.org/10.1016/j.ijfatigue.2016.06.033.
[40] Skorupa M, Korbel A, Skorupa A, Machniewicz T. Observations and analyses of secondary bending for riveted lap joints. Int J Fatigue 2015;72:1–10. https://doi.org/10.1016/j.ijfatigue.2014.10.008.
[41] Zhao L, Xin A, Liu F, Zhang J, Hu N. Secondary bending effects in progressively damaged single-lap, single-bolt composite joints. Results Phys 2016;6:704–11. https://doi.org/10.1016/j.rinp.2016.08.021.
[42] Schijve J, Campoli G, Monaco A. Fatigue of structures and secondary bending in structural elements. Int J Fatigue 2009;31:1111–23. https://doi.org/10.1016/j.ijfatigue.2009.01.009.